PCCP

PAPER

View Article Online
View Journal | View Issue

Cite this: *Phys. Chem. Chem. Phys.*, 2020, **22**, 313

Atomic arrangement in CuZr-based metallic glass composites under tensile deformation

Huali Hao,[a] Wenzhao Zhou,[b] Yang Lu [bc] and Denvid Lau [ad]*

Received 4th September 2019,
Accepted 21st November 2019

DOI: 10.1039/c9cp04914b

rsc.li/pccp

Lacking macroscopic plasticity severely limits structure applications of bulk metallic glasses (BMGs). In general, particle-reinforced BMGs have an enhanced ductility but show reduced strength, whereas body-centered-cubic CuZr phase (B2 phase)-reinforced bulk MGs display improved ductility and strength. The underlying reason for the improvement in B2 phase-reinforced BMGs is still ambiguous. Herein, the atomic arrangement in $Cu_{48}Zr_{48}Al_4$ BMGs with and without the B2 phase under tensile deformation is studied using molecular dynamics simulation. Different from pure MG where shear transformation zones (STZs) are activated along the same direction to form the domain shear band, STZs in the B2 phase-reinforced MG are activated along different directions disturbing the formation of a domain shear band. More plastic deformation and increased stress are allowed because of the phase transformations of B2 phases. The revealed deformation mechanism of B2 phase-reinforced MGs enables us to design heterogeneous structures with excellent strength and toughness.

Introduction

Metallic glasses (MGs) have attracted substantial attention and been considered potential candidates for applications in the fields of microelectromechanical systems, nanoelectromechanical systems, biomedical implants, precious microparts, surgical tools, and micromachines due to their high strength and hardness, large elastic strain, outstanding corrosion resistance, and good wear resistance.[1–5] Although nanoscale MGs can have a high ductility, the deformation of bulk MGs is attributed to the localization of plastic strain to shear bands, causing bulk MGs to exhibit little extensibility under ambient tension where the ductility is less than 0.5%.[6–8] Bulk MGs can fail catastrophically along a single domain shear band that evolves into a crack at vanishingly small tensile strain, limiting the reliability of MGs and their potential engineering applications.[9–14]

In recent years, crystalline phases are *in situ* or *ex situ* induced to improve the tensile ductility of bulk MGs by inhibiting the rapid propagation of domain shear bands. For example, extrinsic crystalline phases such as TiC, TiB, WC, ZrC or ZrO_2, dendrites (a tree-like crystalline structure) and crystalline phases that undergo the diffusionless phase transformation during plastic deformation can improve ductility to more than 5%.[15–18] It has been reported that the improved ductility in the extrinsic phase and dendrite-reinforced MGs associates with work-softening, whereas a diffusionless phase transformation during plastic deformation can significantly enhance the ductility of MGs accompanied with obvious work-hardening.[19–21] Up to now, the discovered parent phase with diffusionless transformation in the MG matrix is only the equiatomic CuZr intermetallic compound with a body-centered-cubic (bcc) structure (B2 phase).[22,23] This new kind of an MG composite with improvements both in tensile ductility and strength provides a novel approach for designing practical MGs with excellent performance. However, the underlying reason for the enhancements in both the tensile ductility and strength in a crystalline phase with martensitic transformation-reinforced MGs is still ambiguous. A thorough understanding of the atomic arrangement in MGs with and without the B2 phase during tensile deformation enables us to figure out the underlying reason for the excellent performance of B2 phase-reinforced MGs.

It is noticeable that the plastic deformation of MGs and crystalline phases are dominant through different mechanisms. The plastic deformation of crystalline structures is normally accomplished through the motion and production of dislocations that are the result of the rupture of the atomic bonds along a line in the lattice.[24–26] Moreover, the B2 phase is plastically deformed with a new monoclinic ZrCu phase (B19′ phase) formed by diffusionless transformation under the shear strain.[27,28] In contrast to conventional crystalline materials deforming plastically through dislocation activity and phase transformation, plastic deformation of MGs occurs through the

[a] *Department of Architecture and Civil Engineering, City University of Hong Kong, Hong Kong, China*
[b] *Nanomanufacturing Lab, Centre for Advanced Structural Materials, Shenzhen Research Institute of City University of Hong Kong, Shenzhen 518057, China*
[c] *Department of Mechanical Engineering, City University of Hong Kong, Hong Kong, China*
[d] *Department of Civil and Environmental Engineering, Massachusetts Institute of Technology, Cambridge, Massachusetts 02139, USA. E-mail: denvid@mit.edu*

activation of the shear transformation zones (STZs).[29–31] STZs experiencing the largest nonaffine strain are preferentially activated in the matrix involving weakly bonded atoms, and coalesce from tens of atoms to hundreds of atoms.[32,33] The STZs behave as Eshelby inclusions where the matrix exhibits a quadrupolar deformation symmetry and the inclusions represent the size of STZs.[34] STZs have the highest atomistic strains, whereas the matrix surrounding the STZs displays the lowest strain and relatively higher stresses.[35] The percolation of STZs along a plane of maximum shear stress causes the formation of a domain shear band.[36] The domain shear band has a highly localized plastic flow and propagates rapidly, resulting in the low tensile ductility of MGs.[32] On one hand, compared to heterogeneous materials made up of nanocrystals,[37] the interface that can significantly affect the crack propagation between adjacent phases also plays a significant role in the enhanced mechanics in crystalline phase-reinforced MGs. On the other hand, the orientation of adjacent crystals determines the crack propagation in heterogeneous materials made up of nanocrystals, whereas the structure of MGs near the interface significantly affects the crack propagation path in crystalline phase-reinforced MGs. This is because the structure of MGs is heterogeneous with different atom packing densities. The crack is prone to propagation in the region having a low packing density causing minimized energy dissipated. The coordination and interactions of different plastic behaviors in the B2 phase-reinforced MGs should be revealed in order to shed light on their deformation mechanism.

The objective of this study is to investigate the interactions between the crystalline and glassy structures in the B2 phase-reinforced $Cu_{48}Zr_{48}Al_4$ MGs under tensile deformation. The underlying cause for the failure of this composite has been analyzed to determine a way to enhance both tensile strength and ductility. First, $Cu_{48}Zr_{48}Al_4$ MGs with and without the B2 phase have been constructed, which suffer from uniaxial tensile deformation at a fixed strain of 10^{-2} ps^{-1} at 50 K. Subsequently, the atomistic local strain during the deformation of different modeled structures is characterized to determine whether the STZs activated in the amorphous matrix. The effect of the crystalline structure on the atomic rearrangement in the amorphous matrix is analyzed by comparing the atom displacement in two-modeled structures. Our study reveals the relationship between the structural evolution and mechanical response in the B2 phase-reinforced MGs under tensile deformation and figures out the underlying reason for the improvement of strength and ductility. Our revealed failure mechanism can provide an insight into the design and fabrication of new heterogeneous materials that have outstanding strength and ductility and can be practically applied.

Simulation methodology

Methods

The molecular simulations are performed using a large-scale atomic/molecular massively parallel simulator (LAMMPS).[38] A developed embedded-atom method (EAM) potential for the Cu–Zr–Al ternary system based on the *ab initio* calculations has been successfully applied to predict the properties of configurations, such as the crystalline phase, liquids and metallic glasses (MGs), and the EAM-derived results are comparable with both *ab initio* and experimental data.[39–41] The total energy of a solid in EAM is a unique function of electron density, where the total energy of a system is approximated as:[39,42]

$$E = \sum_i E_i$$
$$E_i = F_\alpha\left(\sum_{j\neq i}\rho_\beta(R_{ij}) + \frac{1}{2}\sum_{j\neq i}\Phi_{\alpha\beta}(R_{ij})\right) \quad (1)$$

where F is the embedding energy, which is a function of the atomic electron density ρ; $\Phi(r_{ij})$ is the pair interaction between atoms i and j separated by a distance r_{ij}. This potential has accurately predicted the structure of CuZrAl MGs where the pair distribution function results of the modeled MG predicted by the EAM potential are in good agreement with the X-ray results measured from the experiment.[43] The EAM potential has also successfully predicted the phase transformation of the CuZr phase under deformation and this result is also in good agreement with experimental results.[44] The cohesive energy of the CuZr phase predicted by EAM potential is about −5.07 eV per atom, which is similar to the value −5.06 eV per atom obtained from *ab initio* calculations.[43] Considering these, EAM potential is selected to describe the interatomic interactions in $Cu_{48}Zr_{48}Al_4$ MGs, B2 phase and at the interface between MG and B2 phases system is melted and equilibrated for 10 ns in the isothermal–isobaric (*NPT*) ensemble at 0 Pa and 2400 K, which is above the melting point of the amorphous alloy. The modeled system is then cooled at a cooling rate of 10 K ns^{-1} from 2400 K to 50 K and run in the *NPT* ensemble at 0 Pa and 50 K for another 10 ns, obtaining the configuration of the $Cu_{48}Zr_{48}Al_4$ MG. The temperature of the *NPT* ensemble used for these processes is controlled by a Nose–Hoover thermostat, and the pressure was controlled at zero using a Nose–Hoover barostat. The B2 phase has a lattice constant of 0.33 nm. The timestep used is 1 fs. If a large timestep is used, the motion of particles becomes unstable due to the big truncation error in the integration process, the total energy of the system rapidly increasing with time. The molecular dynamics integration algorithm becomes unstable at a large timestep size. If the timestep is too small, it is inefficient because it takes a very long running time. The default value of timestep for the metal atoms in the LAMMPS is 1 fs. The periodic boundary conditions is applied to three directions of modeled $Cu_{48}Zr_{48}Al_4$ MG and B2 phase respectively. Specifically, the x, y and z directions are parallel to the [100], [010] and [001] directions of the crystalline B2 phase. By examining the root-mean-square displacement (RMSD) of atoms, which keeps at a constant level before the 200 ps *NVT* equilibrium run completes at different temperatures, it implies that the equilibrated state has been obtained. The glass transition temperature and radial distribution function of the modeled $Cu_{48}Zr_{48}Al_4$ MG and Young's modulus of the B2 phase

have been predicted. The B2 phase is embedded into an amorphous matrix to construct the B2 phase-reinforced MG structure. The volume fraction of the B2 phase is about 34%. The modeled $Cu_{48}Zr_{48}Al_4$ MG has a size of 46 nm × 5 nm × 110 nm, and the size of the modeled $Cu_{48}Zr_{48}Al_4$ MG with the B2 phase is 46 nm × 5 nm × 110 nm. During the tensile deformation, a periodic boundary condition is applied to the y and z directions of the MG matrix and a free boundary condition is applied to the x direction to allow the occurrence of shear offset on the free surfaces. The modeled systems are deformed by applying a constant and uniaxial strain rate along the z-coordinate at different temperatures. The atomistic strain tensor (η_i) is defined as $\eta_i = (J_i J_i^T - I)/2$, where J_i denotes the local deformation gradient tensor.[45] To visualize plastic shearing during deformation, the local shear strain (or local shear invariant von Mises strain) of each atom i in the system is calculated using the equation:[46,47]

$$\eta_i^{\text{Mises}} = \sqrt{\frac{1}{6}\left[\left(\eta_{xx}-\eta_{yy}\right)^2+\left(\eta_{yy}-\eta_{zz}\right)^2+(\eta_{zz}-\eta_{xx})^2+\eta_{xy}{}^2+\eta_{yz}{}^2+\eta_{zx}{}^2\right]} \quad (2)$$

where η_{xx}, η_{yy}, η_{zz}, η_{xy}, η_{yz} and η_{zx} are the components of the Lagrangian strain matrix for a specific atom. To calculate the η^{Mises} of each atom, the individual atomic positions after deformation are compared with their corresponding configurations in the non-deformed forms by ignoring the homogeneous deformation. The local shear strain in the STZs is reduced from the center of the STZs to the outer area, and the matrix surrounding STZs has a minimized local shear strain.[34,48] The matrix, consisting of atoms with large enough η^{Mises}, can be regarded as the STZ. To visualize the atomic structure and the atomic-scale deformation mechanisms, we use the OVITO software.[49]

Physical and mechanical properties predicted by the EAM potential

The physical and mechanical properties of $Cu_{48}Zr_{48}Al_4$ MGs and the B2 phase are predicted by the EAM potential. Fig. 1 shows the temperature dependence of the specific volume for the $Cu_{48}Zr_{48}Al_4$ MGs during the cooling process. The specific volume continuously changes with temperature, indicating the formation of a glassy structure for the $Cu_{48}Zr_{48}Al_4$ liquid at a cooling rate of 0.01 K ps^{-1}. The intersect of the extrapolations for the undercooled melt and the metallic glass lines denote the glass transition temperature (T_g) of $Cu_{48}Zr_{48}Al_4$ of about 712 K, which is slightly higher than the experimental value of 688 K.[50] The simulated T_g is reasonable in comparison with the experimental one considering the much higher cooling rate in the simulation than that in the experiment.[51] The radial distribution function (RDF) analysis is among one of the most important methods to reveal the structural features of a system, particularly for liquids and amorphous structures.[52] Fig. 2 shows the total and partial RDF of the $Cu_{48}Zr_{48}Al_4$ MG. After the simulated

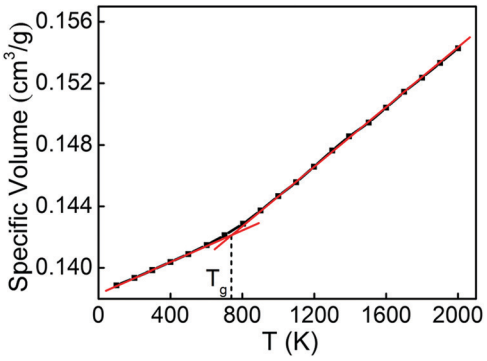

Fig. 1 Specific volume as a function of temperature $Cu_{48}Zr_{48}Al_4$ liquid at a cooling rate of 0.01 K ps^{-1}. The red lines are the linear fit. The glass transition temperature (T_g) is determined from the intersection of the two red lines.

system is cooled down from the liquid state to the glassy state, the second peak of RDF for the $Cu_{48}Zr_{48}Al_4$ MG is split into two peaks, as shown in Fig. 2a. The emergence of the subpeak on the second peak is generally a signal of the local ordering in the amorphous structure, implying the formation of a glassy state.[53] Furthermore, the nearest neighbor distance (the first peak) of RDF for the $Cu_{48}Zr_{48}Al_4$ MG is about 2.75. This has a good agreement with the value (2.71) of the structure factor for the $Cu_{48}Zr_{48}Al_4$ MGs measured *via* X-ray diffraction.[54] Here, the structure factor is sine Fourier transformed to obtain RDF.[55] The atomistic radii of the Cu, Zr and Al atoms determined from the first peak positions of the Cu–Cu, Zr–Zr, and Al–Al curves are 2.55, 3.15, and 2.85, respectively, as shown in Fig. 2b. This is in good agreement with the experimental data, where the atomistic radii of the Cu, Zr and Al atoms are 2.56, 3.14 and 2.86, respectively, suggesting that the EAM potential is appropriate for expressing the real force filed in the Cu–Zr–Al system. The Young's modulus (E) of the B2 phase is also predicted by the MD simulation, which is about 85.4 GPa. The predicted E of the modeled materials is closer to that predicted in the experimental data, where the experimental E of the B2 phase is 82.0 GPa.[56,57] The simulation result of E is higher than the experimental values. This is because the strain rate in the MD simulation is several orders of magnitude higher, making less contribution of thermal motions to the mechanical response of the material. In addition, the constructed model is free of structural defects and voids, which normally exist in the macroscopic samples. All these result in the overestimation of elastic moduli. The error between the simulation results and the experimental values is less than 5%. This indicates the reliability of the EAM potential to predict the mechanical properties of CuZr materials.

Results and discussion

Effect of temperature and strain rate on the tensile behavior of modeled MGs

Fig. 3 shows the stress–strain curves of modeled $Cu_{48}Zr_{48}Al_4$ MGs under the uniaxial tensile deformation of a fixed strain at

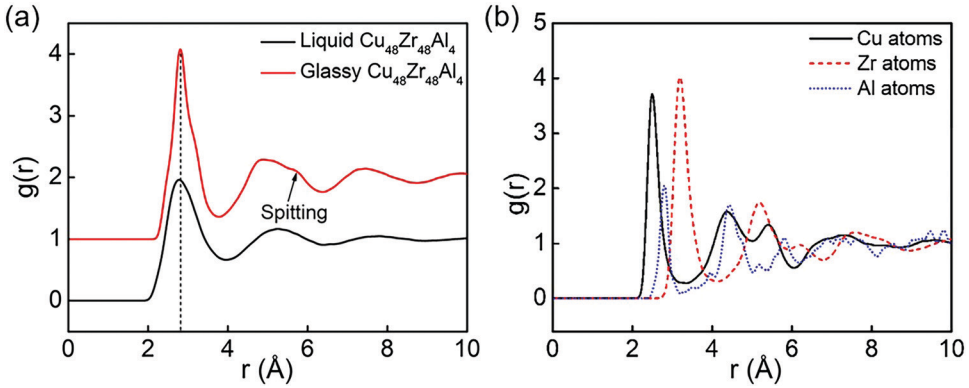

Fig. 2 (a) Total pair distribution function for $Cu_{48}Zr_{48}Al_4$ obtained by MD with EAM potential; (b) partial RDF of $Cu_{48}Zr_{48}Al_4$ MG configuration predicted by MD with EAM potential.

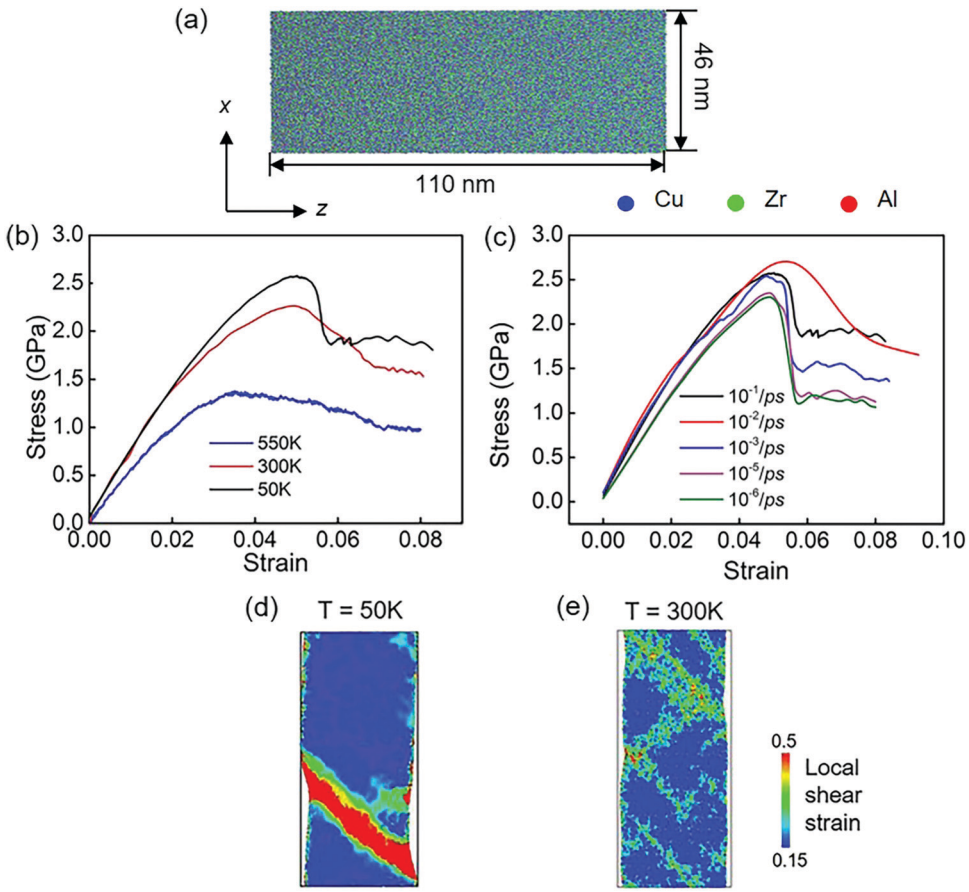

Fig. 3 (a) Initial structure of modeled $Cu_{48}Zr_{48}Al_4$ MGs. (b) The stress–strain response of modeled $Cu_{48}Zr_{48}Al_4$ MGs under the uniaxial tensile deformation of a fixed strain rate of 10^{-2} ps^{-1} at different temperatures. The failure model of MGs is changed at different temperatures. (c) The stress–strain curve of modeled $Cu_{48}Zr_{48}Al_4$ MGs at a low temperature of 50 K under different strain rates. The stress is rapidly reduced at a strain rate smaller than 10^{-2} ps^{-1}, whereas it is gradually reduced at a strain rate higher than 10^{-2} ps^{-1}. The local shear strain distribution at strain of 6% under a strain rate of 10^{-2} ps^{-1} (d) at 50 K; the MG is inhomogeneously deformed with the strain mainly limited in shear band. (e) At 300 K; with the increment of temperature, the modeled MG plastically deforms after yielding. The higher the temperature, the more homogeneous the plastic deformation. Moreover, the yield stress is reduced with the increment of temperature.

different temperatures below the glass transition temperature. It is found that at a low temperature of 50 K, the modeled MG failed because of the inhomogeneous deformation where the strain is mainly limited in the domain shear band, whereas with an increase in temperature, the plastic deformation becomes homogeneous, as shown in Fig. 3b. This indicates that the failure mechanism depends on the temperature because the cooling rate to obtain the glassy structure in the MD simulation can be several

orders of magnitude higher compared with that in the experiment. Such a fast cooling rate does not provide enough time for structure relaxation.[14] The shorter time of diffusion in modeled MGs reduce the distance between two neighbor atoms in MGs constructed in the MD simulation at 300 K, which is smaller than that in MGs fabricated in the experiments at 300 K. The structure of modeled MG at 300 K is much unstable compared with the structure of MG fabricated in the experiment. In the MD simulation, it takes more than one month to obtain the glassy structure at the similar cooling rate to that of the experiment. We reduce the temperature to 50 K to give enough time for the structure relaxation. Moreover, the short-range-ordered structures of MG that have a detrimental effect on the mechanical properties at different temperatures are quantified. It is found that when the temperature is below the glass transition temperature, it has a negligible effect on the short-range-ordered structure of MGs. Therefore, the atomistic structure of the modeled MGs at 50 K is comparable with the structure of MGs obtained in the experiment at 300 K. Our simulation results for the stress–strain response also indicate that the modeled MG failed by inhomogeneous deformation at 50 K, which is consistent with the failure mode of MG fabricated in the experiment at 300 K. In simulation, when the temperature is increased to 300 K, the failure mode is changed with a homogeneous plastic deformation. Taking all these into consideration, the structural evolution of modeled MGs at 50 K gives an insight to understand the structural evolution of MG experimentally obtained at 300 K. Fig. 3c shows the stress–strain response of modeled $Cu_{48}Zr_{48}Al_4$ MGs at 50 K under the uniaxial tensile deformation at different strain rates. The strain rate can also affect the failure mechanism of modeled $Cu_{48}Zr_{48}Al_4$ MGs. A too high strain rate can promote the flow of atoms. When the strain rate is smaller than 10^{-2} ps^{-1}, the stress is rapidly reduced related to the formation of shear bands. When the strain rate is larger than 10^{-2} ps^{-1}, the stress is gradually reduced with a relatively homogeneous plastic deformation. Moreover, it is found that the stress–strain rate at 10^{-5} ps^{-1} is very close to that at 10^{-6} ps^{-1}. This indicates that a reduced strain rate lower than 10^{-5} ps^{-1} does not have a significant effect on the stress–strain curve. The simulated results at 10^{-5} ps^{-1} can be identical to the experimental results. When the strain rate is increased to 10^{-2} ps^{-1}, the strain rate affects the value of stress, but it has no effect on the critical strain when the stress is significantly changed. This means that the stress–strain curve at a strain rate of 10^{-2} ps^{-1} can also reflect the experimental results. Considering the computational cost, the strain rate of 10^{-2} ps^{-1} is a cutoff for the different deformation mechanisms of MGs. The selected strain rate of 10^{-2} ps^{-1} can ensure a similar deformation mechanism obtained from the experiments.

In order to understand the atomic arrangement under tensile deformation and to reveal its failure mechanism, the local shear strain evolution of the $Cu_{48}Zr_{48}Al_4$ MGs at 50 K under the fixed strain rate of 10^{-2} ps^{-1} is shown in Fig. 4. The isolated STZs are activated before the stress reduces, as shown in Fig. 4a. With the strain increased, the STZs with the density increased percolated along the plane with the maximum shear stress (Fig. 4b). A dominant shear band formed as a result of activation, percolation and annihilation of STZs (Fig. 4c). This shear band propagates rapidly along the direction of an angle of 45° with respect to the tensile axis causing the failure of MGs. With the strain increased to more than 6%, the size of the shear band and shear offset increased (Fig. 4d). After the domain shear band is formed, the upper and lower parts of the MG samples slip oppositely along the shear plane causing the shear offset to increase. The energy accumulation during shear sliding leads to an increase in the heat energy in the shear band.[58] The increased heat energy can affect the critical shear stress required for the slip, causing the fluctuation of the stress during the shear sliding. The atom displacement at different deformation stages without considering the homogeneous deformation is also represented in order to explain how the STZs are activated and percolated. The atoms first move under shear stress. As the homogeneous displacement along the tensile direction is not considered, the motion of atoms is perpendicular to the tensile axis (Fig. 4e). The activated STZs significantly deflect the surrounding matrix motion making it to displace preferentially on the plane with the maximum shear stress (Fig. 4f). The motion of atoms in the STZs is random, whereas the atoms near the STZs have a vortex-like motion. A strong antisymmetric strain field can be generated near the STZs and the following STZs along the plane with maximum shear stress are activated when the local stress exceeds a threshold value. The increased STZs can significantly disturb the vortex-like motion of the surrounding matrix, resulting in the percolation and annihilation of individual STZs. Eventually, a domain shear band is formed, and the matrix near the domain shear band eventually displaces along the direction with maximum shear stress (Fig. 4g). Moreover, for the STZs with a minimum stress,[59] the significant increase in both the density and size of STZs can cause a reduction in the stress response for $Cu_{48}Zr_{48}Al_4$ MGs. The local temperature of the shear band region is quantified. It is found that when the domain shear band is formed, the local temperature of the shear band increased along with the increment in the overall strain (Fig. 4h). This is because, after the domain shear band is formed, the upper and lower parts of the MG samples slip oppositely along the shear plane causing the shear offset. The shear stress required to slide on the slip plane along the slip direction is constant; the stress almost remained constant during the slip. The energy accumulation during shear sliding leads to an increase in the temperature in shear bands. The increased temperature can affect the critical shear stress required for the slip causing fluctuation in the stress.

Stress response of $Cu_{48}Zr_{48}Al_4$ MGs with embedded B2 phase

Fig. 5 shows the stress–strain response of MGs with embedded B phases at 50 K at a fixed strain rate of 10^{-2} ps^{-1}. The [001] direction of the B2 phase is tilted to increase the angle between the tensile direction and the [001] direction of the B2 phase. In these 4 samples, the tensile direction is parallel to the [001], [112], and [111] directions of the B2 phase, respectively. Different from the tensile behavior of $Cu_{48}Zr_{48}Al_4$ MG, where there is a nearly linear stress–strain relationship before the stress drops

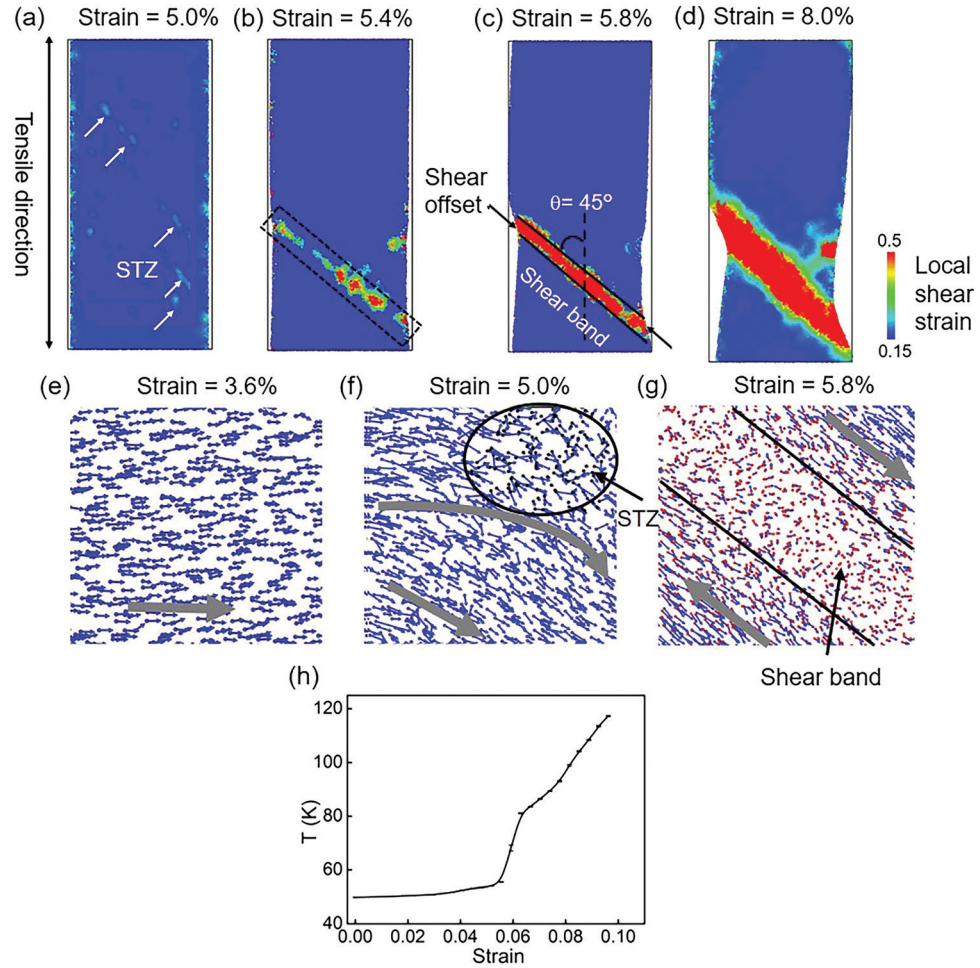

Fig. 4 Local shear strain distribution of the modeled $Cu_{48}Zr_{48}Al_4$ MG at different strains of: (a) 5.0% where the STZs are activated. (b) 5.4% where more STZs are activated and they coalesce. (c) 5.8% where a domain shear band is formed. the shear band caused the fast failure of MGs is along the direction of an angle 45° with respect to the tensile direction. (d) 8.0% where the size of shear band and shear offset is increased. The shear offset is obviously observed. The atom displacement at the different strain of (e) 3.6% where the atom is moved perpendicularly without considering the homogeneous displacement. (f) 5.0% where the motion direction around the activated STZs is obviously rotated. (g) 5.8% where the atoms near the domain shear band move along the direction of maximum shear stress. (h) The temperature changes of the shear band region surrounded by dotted rectangles in (b) with strain.

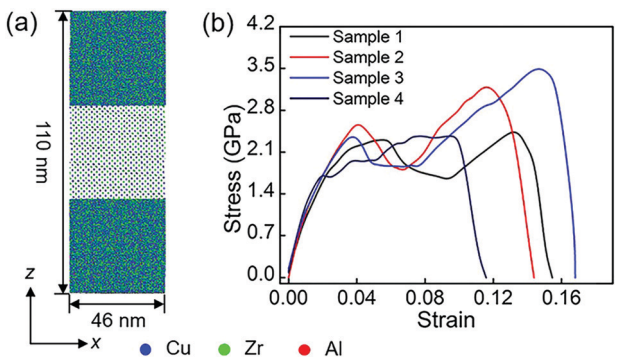

Fig. 5 (a) Initial structure of modeled $Cu_{48}Zr_{48}Al_4$ MGs. (b) Stress–strain curve of modeled MGs with B2 phase where the tensile direction is along different lattice orientation of the B2 phase. After yielding, the samples display work-hardening before fracture. compared with pure MGs, the ductility of MGs with embedded B2 phase is increased.

precipitously at a strain of about 5.0%, the stress of the modeled $Cu_{48}Zr_{48}Al_4$ MG with the B2 phase is reduced after yielding followed by work-hardening before reaching the peak. The ductility is obviously increased compared with that of MGs. As the volume fraction of the crystalline phase was kept unchanged in different samples, the Young's modulus remained nearly constant. Table 1 shows the yield strength, the

Table 1 The yield strength, the ultimate strengths and elongation of modeled MGs with the B2 phase. The [001] direction of the B2 phase is tilted to increase the angle between the tensile direction and the [001] direction of the B2 phase

		35°	45°	55°	
Sample	1	2	3	4	Average
Yield strength (GPa)	2.20	2.34	2.24	1.42	2.05 ± 0.4
Ultimate strength (GPa)	2.48	3.17	3.30	2.41	2.84 ± 0.37
Elongation (%)	13.2	12.7	13.7	10.6	12.8 ± 1.18

Table 2 The Schmid factor, slip systems and $\cos\lambda$ of the B2 phase in different samples

Tensile direction	$\cos\lambda$	Schmid factor for slip	Slip systems		$\cos\varphi$ on (101) plane
			Slip directions	Slip plane	
z [001]	0.33	0.47	⟨111⟩	{112}	0.71
z [112]	0.47	0.41	[1$\bar{1}$1], [$\bar{1}$11]	(101), (011)	0.87
z [10$\bar{1}$]	0.82	0.41	[11$\bar{1}$], [1$\bar{1}\bar{1}$], [$\bar{1}\bar{1}$1], [$\bar{1}$1$\bar{1}$]	(01$\bar{1}$), (110), (1$\bar{1}$0), (011)	0
z [111]	1	0.47	[111]	($\bar{1}$12), (1$\bar{1}$2)	0.82

ultimate strength and elongation of different samples. The yield strength, ultimate strength and elongation are highly dependent on the orientation. As the amorphous matrix undergoes homogeneous deformation in MGs with the B2 phase, the yielding of MGs with the B2 phase is a result of the yielding of the B2 phase. The crystalline phase is plastically deformed by slipping on the plane with the highest atom packing density and along the direction with the highest atom packing density, because minimized stress is required for the motion of dislocations on such plane and along such directions. As the B2 phase has the body-centered-cubic structure, it can slip on the {110} and {112} planes along the ⟨111⟩ directions. The restored shear stress (τ) can be expressed as:[60]

$$\tau = \sigma \cos\lambda \cos\varphi \quad (3)$$

where τ is the applied tensile stress, φ is the angle between the normal direction of the slip plane and tensile direction, and λ is the corresponding angle between the slip direction and the tensile axis. The critical stress required to cause yielding is a function of $\cos\varphi\cos\lambda$ (named the Schmid factor). Table 2 shows a summary of the Schmid factor, slip systems and $\cos\lambda$ of the B2 phase in different samples. It is clear that larger the

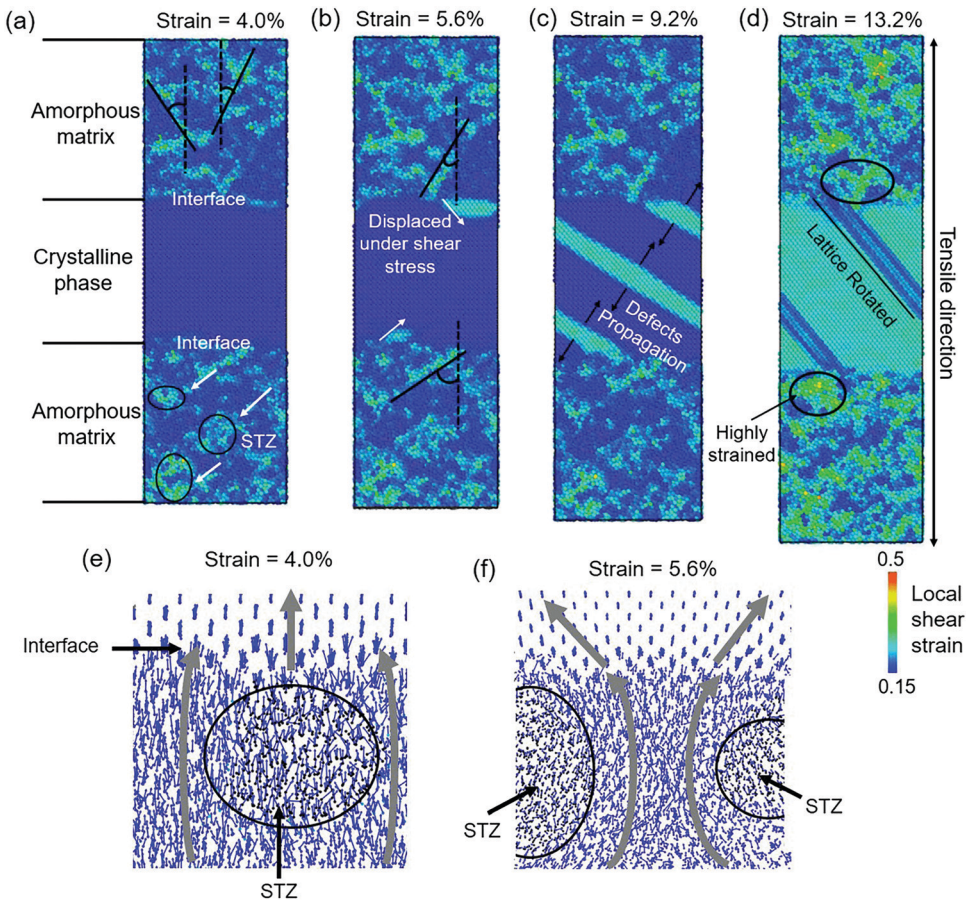

Fig. 6 Local shear strain distribution of the modeled $Cu_{48}Zr_{48}Al_4$ MG with B2 phase at different strains of (a) 4.0% where the STZs in the amorphous matrix are activated. The STZs are not activated along the direction of an angle 45° with respect to the tensile direction. (b) 5.6% where the crystalline structure near the interface is highly strained. (c) 9.2% where the crystalline structure is deformed with the phase transformation. (d) 13.2% where a new phase is formed associating with the rotation of the crystalline structure. The amorphous matrix is highly strained. The atom displacement at the different strain of (e) 4.0% where the atoms' motion in the amorphous matrix near the interface are deflected causing the atoms in the crystalline structure close to the interface displaced nearly along the tensile direction. (f) 5.6% where more STZs near the interface are activated resulting in the atom in the crystalline structure move along the orientation of maximum shear stress (direction of an angle of 45° with respect to the tensile axis).

Schmid factor, lower is the value of applied stress σ required for the slip. This indicates that there is a lower yield strength in the samples, where the crystalline phase has a higher Schmid factor. When the Schmid factor is similar in samples, a high value of $\cos\lambda$ means a higher shear stress along the slip direction promoting the slip. Therefore, for samples with a similar Schmid factor, there is a lower yield strength in the samples with a larger value of $\cos\lambda$. This is the reason that there is a minimized yield strength in the sample where the tensile direction is parallel to the [111] direction of B2 phases, whereas there is a maximum yield strength in the sample, where the tensile direction is parallel to the [112] direction of the B2 phases.

The phase transformation of the B2 phase occurs in the (101) plane direction. The stress on the (101) plane is determined by $\cos\varphi$. A large $\cos\varphi$ indicates a large stress on the (101) plane. The failure of the sample is due to the high stress concentration near the interface contributing to the formation of pores. The large stress in the (101) plane promotes the phase transformation of the B2 phase and the formation of pores resulting in a low elongation. Therefore, there is a low elongation in samples where the tensile direction is parallel to the [112] and [111] directions. The slip systems can interfere with each other causing a difficulty in the slip movement. These interactions among slip systems contribute to the improvement in the ultimate strength. A higher ultimate strength can be

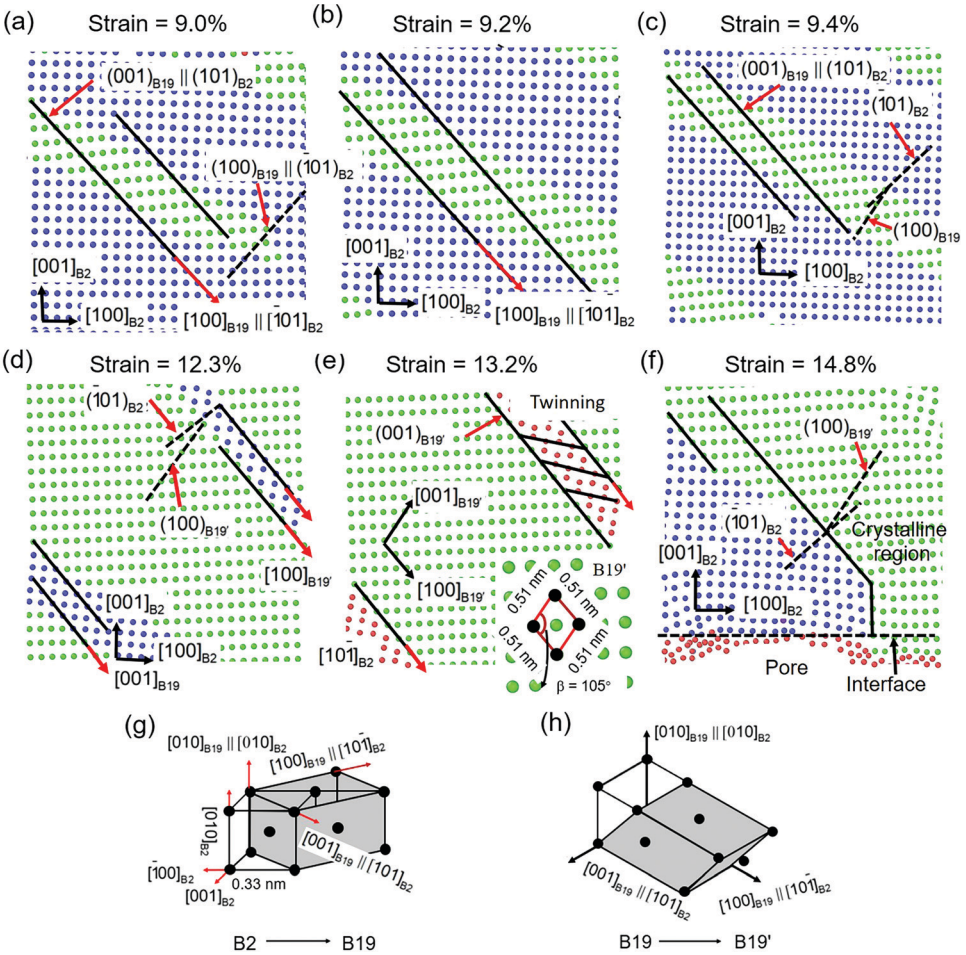

Fig. 7 Structural evolution of the crystalline phase at different strains of (a) 9.0% where a new B19 phase is generated to relax the high strain stored in the crystalline structure. The B19 phase of the orthonormal structure is formed by shear of the basal plane (101)B2 along [10$\bar{1}$]B2 direction. (b) 9.2% where the formed B19 phase is grown along the crystalline orientation [10$\bar{1}$]B2. This growth causes the rotation of the basal B2 phase where the plane (10$\bar{1}$)B2 is not parallel to the (100)B19 plane as the dot lines shown. (c) 9.4% where the growth orientation of B19 phase is twisted because of the shear on (010)B2 plane along [101$\bar{1}$]B2 direction. The planes (10$\bar{1}$)B2 and (100)B19 are not parallel because of the rotation of B2 structure on (010) plane. (d) 12.3% where the B19 phase transforms to monoclinic B19′ phase. The angle between (10$\bar{1}$)B2 and (100)B19 is increased. (e) 13.2% where the twins are formed to coordinate the neighbor B19′ phases. (f) 14.8% where a pore is formed at the interface to relax the stress concentration. This relaxation results in the formed B19′ phase reversibly transforms into B2 phase. (g) The details of B2 phase transforms to B19 phase by the shear on (101)B2 plane along [10$\bar{1}$]B2 direction. The formed B19 phase has a relationship with the basal B2 structure that [100]B19 is parallel to [10$\bar{1}$]B2, [010]B19 is parallel to [010]B2 and [001]B19 is parallel to [101]B2. The orientation of the B19 phase is (100)B19 parallel to (10$\bar{1}$)B2. (h) The details of B19 phase transformed to B19′ phase by the shear on (010)B2 plane along [10$\bar{1}$]B2 direction. The blue atoms refer to the atoms in the B2 phase, the green atoms mean the atoms in the new formed B19 phase and B19′ phase and the red atoms refer to atoms in the disordered arrangement.

found in samples with a larger number of initial slip systems. The ultimate strength is relatively high in samples where the tensile direction is parallel to [112] and [10$\bar{1}$].

To understand the structural evolution of modeled $Cu_{48}Zr_{48}Al_4$ MGs with the B2 phase during tensile deformation, the sample where the z direction is parallel to the [001] direction of the B2 phase is selected as an example. The local shear strain and atom displacement of the modeled $Cu_{48}Zr_{48}Al_4$ MG with the B2 phase under the tensile deformation are shown in Fig. 6. The STZs are activated in the amorphous matrix similar to that in $Cu_{48}Zr_{48}Al_4$ MGs and the crystalline structure is non-deformed (Fig. 6a), causing a linear stress–strain response. With the strain increased, the neighboring STZs are activated along different planes (Fig. 6b). The crystalline structure is inhomogeneously deformed with a strain relaxation in the amorphous matrix (Fig. 6c). The highly strained crystalline structure is rotated with an increment of the strain (Fig. 6d). Fig. 6e shows the effect of the crystalline structure on the atom motion. The vortex-like motion of the matrix surrounding the STZs is deflected by the interface, resulting in the crystalline structure being displaced nearly along the direction parallel to the tensile axis. A high local strain at the interface promotes the activation of the STZs along the direction parallel to the interface instead of the direction of 45° with respect to the tensile axis (Fig. 6f). The different activation plane of STZs destructs the vortex-like motion in the amorphous matrix preventing the formation of the domain shear band. The highly strained interface is then relaxed by the deformation of the crystalline structure, causing a reduction in the stress response. With the deformation continuing, the stress–strain response is dominant due to the crystalline structure deformation. When the whole crystalline structure has a higher strain than the surrounding amorphous matrix, more STZs are activated and percolated. In turn, the highly strained amorphous matrix can promote the deformation of the crystalline structure. This interaction between the amorphous matrix and crystalline structure results in an improvement of stress with the strain increased.

Interactions between the crystalline phase and the amorphous matrix

Fig. 7 shows the details of the crystalline phase deformation at different strains. Before the stress reduces, the crystalline structure is non-deformed. The large displacement of the crystalline atoms near the interface causes a diffusionless phase transformation from the B2 phase to the orthonormal ZrCu phase (B19 phase). The B19 phase is formed because of the displacement of the B2 phase on the plane (101)B2 along the [101]B2 direction and the (100)B19 plane is parallel to the (10$\bar{1}$)B2 plane, as shown in Fig. 7a. The B19 phase is grown along the [10$\bar{1}$]B2 direction, resulting in the rotation of the B2 phase, and the (100)B19 plane is not parallel to the (10$\bar{1}$)B2 plane, shown as dotted lines in Fig. 7b. This diffusionless phase transformation releases the stress stored in the crystalline structure, causing a decreased stress response. The newly formed B19 phase is deformed because of the shear on the (010)B2 plane along the [10$\bar{1}$]B2 direction, as shown in Fig. 7c. The shear deformation of the B19 phase leads to the formation of the B19′ phase, allowing more plastic deformation and work-hardening. As shown in Fig. 7d, with the increase in strain,

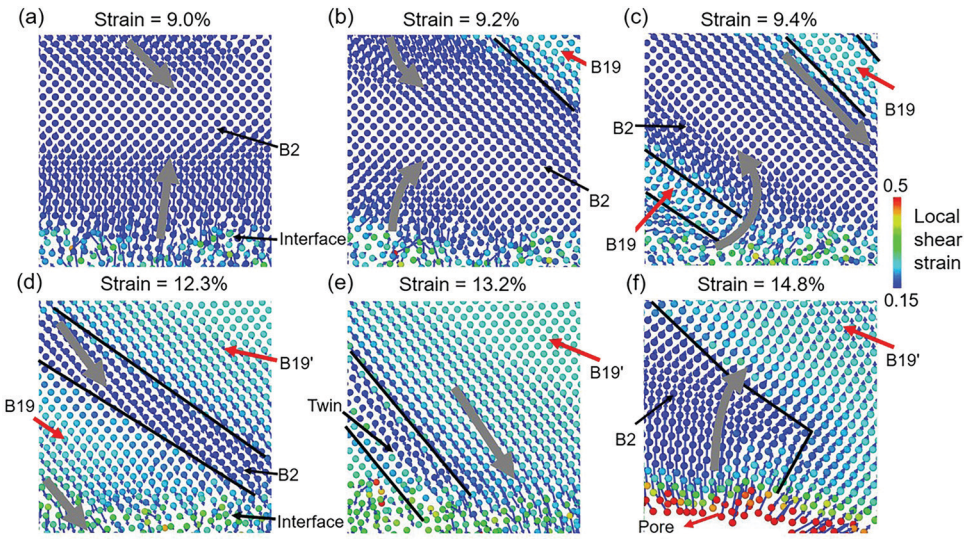

Fig. 8 The displacement of atoms at the interface under different strains (a) 5.6% where the interfacial atoms move nearly parallel to the tensile direction. (b) 9.2% where the atomistic motion near the interface is rotated because of the formation of a new phase. (c) 9.4% where the atoms of B2 phase move along the maximum shear stress direction. The shearing of the basal B2 phase results in the formation of new B19 phase where atoms have no obvious displacement. (d) Atoms in the newly formed phase are displaced to coordinate the deformation because of a significant reduction of B2 phase. (e) When the B2 phase is totally transformed to B19′ phase, the atoms undergo shearing along the same direction resulting in the displacement of atoms at the interface increased. A large displacement of atoms in STZs near the interface increases the free volume resulting in a pore nucleated. (f) The pore generated significantly relaxes the strain and stress stored in the crystalline structure. The displacement of crystalline atoms is obviously reduced with reversing the shearing direction.

more of the B2 phase is transformed to the B19 and B19′ phases. The angle between the (10$\bar{1}$)B2 plane and (100)B19 plane increased due to the rotation of the crystalline structure. When the B2 is totally transformed to the B19′ phase, twins are formed to coordinate the neighboring B19′ phases, as shown in Fig. 7e. The twinning is prevented at the interface, resulting in stress concentration. The interfacial stress concentration facilities the percolation of the STZs. A pore is nucleated at the interface when the free volume of STZs near the interface is over a threshold, as shown in Fig. 7f. The nucleation of the pore leads to strain relaxation, causing the formed B19′ phase to transform reversibly into the B2 phase. Fig. 7g shows the details of the phase transformation from the B2 phase to the B19 phase. It is clear that [100]B19 is parallel to [10$\bar{1}$]B2, [010]B19 is parallel to [010]B2, and [001]B19 is parallel to [101]B2. The phase transformation from the B19 phase to the B19′ phase is shown in Fig. 7h, which is the result of shear on the (010)B2 plane along the [10$\bar{1}$]B2 direction, [001]B19′ is parallel to [101]B2.

The details of interactions between the crystalline structure and the amorphous matrix in $Cu_{48}Zr_{48}Al_4$ MGs with the B2 phase are shown in Fig. 8. Before the deformation of the crystalline structure, the atoms at the interface move parallel to the tensile direction, as shown in Fig. 8a. As the new phase is formed by shear of the basal plane (101)B2 along the [10$\bar{1}$]B2 direction, the motion of atoms surrounding the new phase is obviously rotated toward the direction with the maximum shear stress, as shown in Fig. 8b. As a result of the lattice-invariant shear, there is no displacement for atoms in the newly formed B19 phase, as shown in Fig. 8c. The B2 phase, confined among the newly formed B19 phase, is deformed under shear stress, contributing to the transformation of the B2 phase. With the

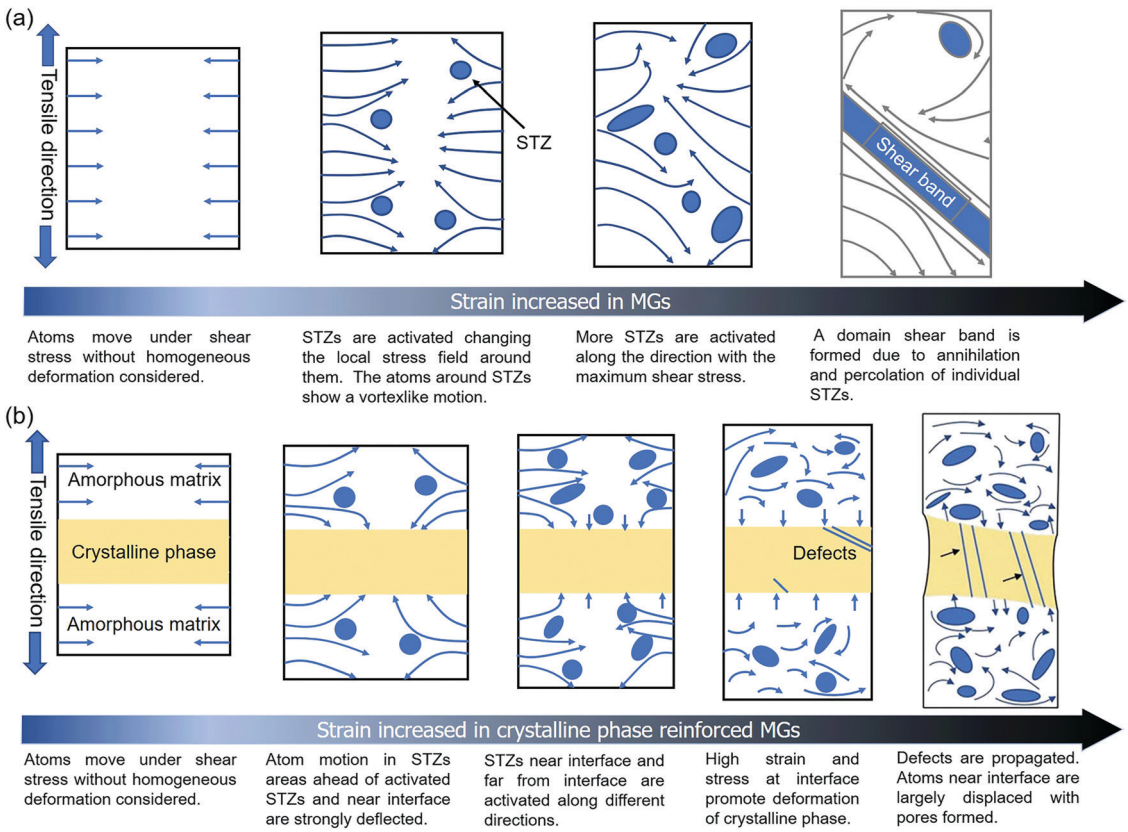

Fig. 9 Schematic diagram of atom motions in the different modeled structures during the tensile deformation of (a) MGs. The homogeneous deformation is not taken into consideration. The atoms firstly suffer from shear stress and the STZs are activated with the strain increased. The motion direction of the atoms around the STZs is significantly rotated. with the increment of strain, the STZs are distorted along the maximum shear direction which has an angle of 45° with respect to tensile direction and more STZs are activated. The obvious torsion of the STZs can cause stress reduction of the MGs. The non-highly deformed atoms display a vortex-like behavior which in return obviously affects the activation and penetration of STZs. A domain shear band causing the fast fracture of the MG is formed under the activation, percolation and annihilation of STZs. (b) MGs with crystalline phase. At the beginning deformation stage, the amorphous matrix mainly suffers from the deformation. The atom motion near the interface is highly deflected because of the crystalline phase affecting the local strain and stress field. The maximum shear stress near the interface and far from the interface in the amorphous matrix is not along a similar direction. This causes the neighbor STZs near and far from the interface along different planes restricting the domain shear band formed. The high strain at the interface is relaxed by the deformation of the crystalline structure which significantly deflects the atomistic displacement at the interface. The propagation of the defects can result in the failure of the crystalline structure, leading to a reduced stress response with limited improved ductility in MGs. The STZs near the interface are suffering from shearing resulting in an increment of free volume in STZs. When the displacement of the atoms in STZs is over a threshold, the pores can be generated providing the failure site of the modeled structures. This combination interaction between the amorphous matrix and crystalline phase results in the improvement of strength and ductility.

decrease in volume of the B2 phase, the newly formed B19 phase surrounding the B2 phase suffers from the shear deformation to transform to the B19′ phase, as shown in Fig. 8d. The displacement of atoms in the B19′ phase and near the interface significantly is increased under the shear, as shown in Fig. 8e. The large displacement of atoms in STZs near the interface promotes the STZs to evolve into a pore. The high strain and stress stored in the crystalline phase are greatly relaxed because of the generation of pores, leading to the stress filed in the crystalline phase significantly reversed, as shown in Fig. 8f. Under the reversed shear stress, the B19′ phase transforms back to the B2 phase. After the failure of the modeled structure, all of the B19′ phase transferred to the B2 phase.

According to the previous statement, we can draw a conclusion that the different stress–strain responses in the modeled MGs without and with the crystalline phase are mainly related to atom displacement. Fig. 9 shows a schematic of atom displacement under tensile deformation, explaining the failure mechanism of MG composites. STZs are activated along the maximum shear stress plane in the MGs, and the atoms around the STZs display a vortex-like motion, as shown in Fig. 9a. The vortex-like motion of the matrix can cause the annihilation of smaller STZs. The percolation of STZs along the plane with the maximum shear stress evolves into a domain shear band, which is the underlying reason for the low tensile ductility of MGs. With the existence of the crystalline phase, the amorphous matrix is deformed first where the vortex-like motion of the atoms in the amorphous matrix near the interface is disturbed, as shown in Fig. 9b. The STZs near and far from the interface are percolated along different planes, avoiding the formation of a domain shear band. The crystalline phase is deformed to relax the high stress stored at the interface, leading to a reduction in the stress response. The propagation of the crystallographic defects can result in the failure of the crystalline phase. As a result, there is a reduction in the stress response and a limited ductility improvement. The increase in stress followed by a decrease with the increase of strain has been observed in the particles (such as TiC and TiB) and the dendrite-reinforced MG matrix. The B2 phase can undergo diffusionless phase transformation under the tensile deformation. This diffusionless phase transformation causes the rotation of the crystalline structure. In contrast to other particle-reinforced MGs where the crystallographic defects are propagated after formation, the B2 phase undergoes phase transformation under shearing, leading to an increment in the deformation ability. Improvements in both the tensile ductility and strength can be obtained. The STZs near the interface suffer from shearing, resulting in an increment in the free volume of STZs. The increased free volume of STZs near the interface provides the sites to nucleate the pores. Our results reveal the underlying reason for the improvement in both the strength and ductility under the tensile deformation of the B2 phase-reinforced MGs by tracing the atom displacement. The growth of the B19 phase under shearing results in stress reduction with a limited increment in the ductility. The B19 phase is transformed to the B19′ phase under shearing, leading to an increment in the stress. The revealed deformation mechanism in this study can motivate us to design and fabricate a practical MG composite with higher tensile ductility and strength. For example, reinforcements with different crystalline structures and strengths can be added into the MG matrix. In addition, our study provides an insight for figuring out the interactions between the crystalline structure and glassy structure, inspiring us to design heterogeneous materials with a good combination of strength and toughness.

Conclusions

In summary, B2 phase-reinforced MGs can overcome the low tensile ductility of MGs without sacrificing the strength to solve the brittleness of bulk MGs without reducing their competition edge. This work has studied the atomic arrangement under the tensile deformation, figuring out the deformation mechanism of the $Cu_{48}Zr_{48}Al_4$ MG without and with the B2 phase using the molecular dynamics simulation. The interactions between the crystalline structure and the amorphous matrix are characterized. The deformation of the amorphous matrix dominates the linear stress–strain response, and the crystalline phase evolution is responsible for the nonlinear stress–strain response of B2 phase-reinforced $Cu_{48}Zr_{48}Al_4$ MGs. When the embedded crystalline phase is tilted, the variation of mechanical properties in MGs with the B2 phase is due to the shear stress required for the slip of the B2 phase change. The revealed deformed mechanism of MGs with and without a crystalline phase enables us to improve the tensile ductility of MGs with work-hardening. Moreover, our findings provide an insight for designing and fabricating MGs with both improved strength and toughness for industrial availability.

Conflicts of interest

There are no conflicts to declare.

Acknowledgements

The authors are grateful to the support from the Research Grants Council (RGC) in Hong Kong through the General Research Fund (GRF) with the Grant No. 11255616, and the funding supporting from Shenzhen Science and Technology Innovation Committee under the grants JCYJ20170413141157573 and JCYJ20170818103206501.

References

1 G. Kumar, P. Neibecker, Y. H. Liu and J. Schroers, *Nat. Commun.*, 2013, 41536.
2 H. Kou, J. Lu and Y. Li, *Adv. Mater.*, 2014, **26**(31), 5518.
3 Q. Wang, Y. Yang, H. Jiang, C. T. Liu, H. H. Ruan and J. Lu, *Sci. Rep.*, 2014, **4**, 4757.
4 E. Ma and J. Ding, *Mater. Today*, 2016, **19**(10), 568–579.
5 Q. Wang, J. J. Liu, Y. F. Ye, T. T. Liu, S. Wang, C. T. Liu, J. Lu and Y. Yang, *Mater. Today*, 2017, **20**(6), 293–300.

6 R. Liontas, M. Jafary-Zadeh, Q. Zeng, Y.-W. Zhang, W. L. Mao and J. R. Greer, *Acta Mater.*, 2016, **118**, 270–285.
7 Y. Zou, P. Kuczera, A. Sologubenko, T. Sumigawa, T. Kitamura, W. Steurer and R. Spolenak, *Nat. Commun.*, 2016, 712261.
8 L. Liu, M. Hasan and G. Kumar, *Nanoscale*, 2014, **6**(4), 2027–2036.
9 M. Wakeda, Y. Shibutani, S. Ogata and J. Park, *Appl. Phys. A: Mater. Sci. Process.*, 2008, **91**(2), 281–285.
10 Y. Yang, J. C. Ye, J. Lu, P. K. Liaw and C. T. Liu, *Appl. Phys. Lett.*, 2010, **96**(1), 011905.
11 L. Wang, H. Bei, Y. F. Gao, Z. P. Lu and T. G. Nieh, *Acta Mater.*, 2011, **59**(7), 2858–2864.
12 B. Gludovatz, M. D. Demetriou, M. Floyd, A. Hohenwarter, W. L. Johnson and R. O. Ritchie, *Proc. Natl. Acad. Sci. U. S. A.*, 2013, **110**(46), 18419–18424.
13 B. Sarac and J. Schroers, *Nat. Commun.*, 2013, 42158.
14 L. Wang, L. Wang, Z. Nie, Y. Ren, Y. Xue, R. Zhu and H. Fu, *Mater. Des.*, 2016, 111473–111481.
15 J. Eckert, J. Das, S. Pauly and C. Duhamel, *J. Mater. Res.*, 2011, **22**(2), 285–301.
16 C. Suryanarayana and N. Al-Aqeeli, *Prog. Mater. Sci.*, 2013, **58**(4), 383–502.
17 J. Qiao, *J. Mater. Sci. Technol.*, 2013, **29**(8), 685–701.
18 X. Su, H. Hu and X. Kong, *ICMSE*, 2017, **275**, 012002.
19 K. K. Song, S. Pauly, Y. Zhang, P. Gargarella, R. Li, N. S. Barekar, U. Kühn, M. Stoica and J. Eckert, *Acta Mater.*, 2011, **59**(17), 6620–6630.
20 Z. Y. Zhang, Y. Wu, J. Zhou, H. Wang, X. J. Liu and Z. P. Lu, *Scr. Mater.*, 2013, **69**(1), 73–76.
21 S. H. Hong, J. T. Kim, H. J. Park, Y. S. Kim, J. M. Park, J. Y. Suh, Y. S. Na, K. R. Lim and K. B. Kim, *Appl. Microsc.*, 2015, **45**(2), 37–43.
22 H. C. Sun, Z. L. Ning, G. Wang, W. Z. Liang, S. Pauly, Y. J. Huang, S. Guo, X. Xue and J. F. Sun, *Sci. Rep.*, 2018, **8**(1), 4651.
23 Y. Feng, W. B. Liao, J. Zheng, L. W. Wang, Y. Zhang, J. Sun and F. Pan, *Nanoscale*, 2017, **9**(40), 15542–15549.
24 J. W. Christian and D. E. Laughlin, *Acta Metall.*, 1988, **36**, 1617–1642.
25 C. G. Andres, F. G. Caballero, C. Capdevila and L. F. Alvarez, *Mater. Charac.*, 2002, **48**, 101–111.
26 M. J. Buehler and T. Ackbarow, *Mater. Today*, 2007, **10**, 46–58.
27 X. Ren and O. Kazuhiro, *Scr. Mater.*, 1998, **38**(11), 1669–1675.
28 K. G. Vishnu and A. Strachan, *Acta Mater.*, 2010, **58**(3), 745–752.
29 J. Langer, *Scr. Mater.*, 2006, **54**(3), 375–379.
30 Y. Q. Cheng, E. Ma and H. W. Sheng, *Phys. Rev. Lett.*, 2009, **102**(24), 245501.
31 Y. C. Hu, P. F. Guan, M. Z. Li, C. T. Liu, Y. Yang, H. Y. Bai and W. H. Wang, *Phys. Rev. B: Condens. Matter Mater. Phys.*, 2016, **93**(21), 214202.
32 J. H. Perepezko, S. D. Imhoff, M. W. Chen, J. Q. Wang and S. Gonzalez, *Proc. Natl. Acad. Sci. U. S. A.*, 2014, **111**(11), 3938–3942.
33 C. Zhong, H. Zhang, Q. P. Cao, X. D. Wang, D. X. Zhang, U. Ramamurty and J. Z. Jiang, *J. Non-Cryst. Solids*, 2016, **445–446**, 61–68.
34 P. h. Cao, H. S. Park and X. Lin, *Phys. Rev. E: Stat., Nonlinear, Soft Matter Phys.*, 2013, **88**, 042402.
35 E. R. Homer and C. A. Schuh, *Acta Mater.*, 2009, **57**(9), 2823–2833.
36 R. Maaß, D. Klaumünzer, G. Villard, P. M. Derlet and J. F. Löffler, *Appl. Phys. Lett.*, 2012, **100**(7), 071904.
37 E. Beniash, C. A. Stifler, C. Y. Sun, G. S. Jung, Z. Qin., M. J. Buehler and P. U. P. A. Gilbert, *Nat. Commun.*, 2019, **10**, 4383.
38 S. Plimpton, *J. Comput. Phys.*, 1995, **117**, 1–19.
39 Y. Q. Cheng, E. Ma and H. W. Sheng, *Phys. Rev. Lett.*, 2009, **102**, 245501.
40 J. G. Wang, Y. C. Hu, P. F. Guan, K. K. Song, L. Wang, G. Wang, Y. Pan, B. Sarac and J. Eckert, *Sci. Rep.*, 2017, **7**, 7076.
41 X. F. Zhang, S. P. Pan, J. W. Qiao and A. D. Lan, *Comput. Mater. Sci.*, 2017, **128**, 343–347.
42 M. Imran, F. Hussain, M. Rashid, Y. Cai and S. A. Ahmad, *Chin. Phys. B*, 2013, **22**, 096101.
43 Y. Q. Cheng and E. Ma, *Prog. Mater. Sci.*, 2011, **56**, 379–473.
44 P. Xue, Y. J. Huang, S. Pauly, S. S. Jiang, S. Guo, H. B. Fan, Z. L. Ning, F. Y. Cao and J. F. Sun, *J. Alloys Compd.*, 2019, **782**, 961–966.
45 M. Jafary-Zadeh, R. Tavakoli, D. J. Srolovitz and Y.-W. Zhang, *Extreme Mech. Lett.*, 2016, **9**, 215–225.
46 S. Kim and S. Ryu, *Sci. Rep.*, 2017, **7**(1), 13472.
47 Z. D. Sha, S. X. Qu, Z. S. Liu, T. J. Wang and H. Gao, *Nano Lett.*, 2015, **15**(10), 7010–7015.
48 M. L. Manning, J. S. Langer and J. M. Carlson, *Phys. Rev. E: Stat., Nonlinear, Soft Matter Phys.*, 2007, 76056106.
49 A. Stukowski, *Modell. Simul. Mater. Sci. Eng.*, 2010, **18**, 015012.
50 Q. Zhang, W. Zhang, G. Xie and A. Inoue, *Mater. Trans.*, 2007, **48**(7), 1626–1630.
51 Y. L. Sun and J. Shen, *J. Non-Cryst. Solids*, 2009, **355**(31-33), 1557–1560.
52 G. Duan, D. Xu, Q. Zhang, G. Zhang, T. Cagin, W. L. Johnson and W. A. Goddard, *Phys. Rev. B: Condens. Matter Mater. Phys.*, 2005, **71**(22), 224208.
53 F. Li, X. J. Liu and Z. P. Lu, *Comput. Mater. Sci.*, 2014, **85**, 147–153.
54 Q. Wang, Y. Yang, H. Jiang, C. T. Liu, H. H. Ruan and J. Lu, *Sci. Rep.*, 2014, **4**, 4757.
55 B. Sarac, A. Bernasconi, J. Wright, M. Stoica, F. Spieckermann, M. Mühlbacher, J. Keckes, X. Bian, G. Wang and J. Eckert, *Mater. Sci. Eng., A*, 2017, **707**, 245–252.
56 Y. Wu, H. Wang, Y. Cheng, X. Liu, X. Hui, T. Nieh, Y. Wang and Z. Lu, *Sci. Rep.*, 2015, **5**, 12137.
57 S. Pauly, G. Liu, G. Wang, U. Kühn, N. Mattern and J. Eckert, *Acta Mater.*, 2009, **57**(18), 5445–5453.
58 Z. Y. Liu, Y. Yang and C. T. Liu, *J. Iron Steel Res. Int.*, 2016, **23**(1), 53–56.
59 D. Sopu, A. Stukowski, M. Stoica and S. Scudino, *Phys. Rev. Lett.*, 2017, **119**(19), 195503.
60 H. C. Sun, Z. L. Ning, G. Wang, W. Z. Liang, S. Pauly, Y. J. Huang, S. Guo, X. Xue and J. F. Sun, *Sci. Rep.*, 2018, **8**(1), 4651.